The Development of a Miniaturised Spectroscopic Reflectance System for Thin-Film Multilayer Thickness Measurements

Néstor Eduardo Sánchez-Arriaga, Aruã Clayton Da Silva, Divya Tiwari,
Windo Hutabarat, Adrian Leyland, Ashutosh Tiwari

***Abstract*—The in-process inspection of multilayer thin-film thickness across the width of a substrate is a requirement in roll-to-roll (R2R) manufacturing. However, the current inspection systems present limitations related to the nature of the techniques, in addition to the low scalability, modularity, high cost and complexity of implementation on the manufacturing floor.**

This work introduces the in-house development of a dimension-reduced and modular, single-sensor reflectometer instrument, enabling precise measurement of individual layers within multilayer coated samples. This work includes the development of a new hardware design integrating a microprocessor, a light source, a logic converter and a spectrometer sensor; additionally, a unique software platform was developed to perform near real-time multilayer coating thickness measurements. Seven electrodeposited samples were created for testing and validation purposes. The results of more than one hundred and thirty measurements per sample show that the thickness of an Indium Tin Oxide (ITO) layer ranged between 125.48 to 138.82 ± 2.87 nm, achieving less than 7% error compared to vendor specifications (specification: 130 nm). Additionally, the thickness measurements from the sensor revealed a linear response of the Poly(3,4-ethylenedioxythiophene):Poly sodium 4-styrene sulfonate (PEDOT:PSS) layer with increasing electrodeposition charge, resulting in thicknesses ranging from 201.47 to 506.03 ± 2.73 nm. The successful thickness single-point measurements lay the foundations for the development multi-sensor array to allow thickness measurements along the full width of coated substrates in R2R manufacturing.

***Index Terms*—reflectometry, sensor, thin film, thickness, flexible electronics, roll-to-roll, solar cells, PEDOT.**

I. INTRODUCTION

THE global utilisation of solar cells is increasing from 1% in 2015 to 25% by 2050 [1]; this has triggered the use of roll-to-roll (R2R) manufacturing processes to scale up solar cell production due to its high-speed and low-cost advantages [2], [3]. However, measuring the coating properties for feedback control purposes, such as coating thickness across the width of a substrate (30 cm standard), remains a challenge for R2R systems due to the inspection techniques' limitations, high cost, low scalability and low modularity [3], [4]. Additionally, newer solar cell generation materials have multiple layers with thickness in the order of nanometres, which must be inspected in real-time in-process conditions.

Spectroscopic Ellipsometry (SE) is a proven in-process technique capable of measuring thin-film multilayers with <100 nm ± 5 nm thickness [5]; however, it requires critical adjustment of the angle of incidence to perform measurements and it is polarisation dependent. Imaging Ellipsometry (IE), can measure thickness <300 nm in real-time, but can not measure multilayers [6].

Other angular-dependent optical techniques can achieve single-layer thickness measurements <500 nm, but they have not been proven with organic photovoltaic materials nor can they achieve multilayer measurements [3], [7]–[9]. Interferometric techniques can also measure the thickness of a coating deposited on flexible materials ranging up to $43.5 \pm 0.7\mu$m; however, they are slow to measure a single point and are highly affected by vibration [11]–[14]. Focus variation microscopy (FVM) is another technique being explored for on-machine measurements; however, FVM is limited to thickness measurements $> 1\mu$m and cannot measure thin-film multilayers; additionally, recent developments make it challenging to adapt to R2R machines for increasing the measurement coverage across the width of substrates [15]. Spectroscopic techniques, in combination with machine-learning, are being explored; however, the nanometric scale of the solar cell layers and the need for data to train machine-learning models could make this process cumbersome [16]–[20]. Eddy current techniques can achieve multilayer thickness measurements ranging 31 - 406 ± 5 nm; however, they do not work on insulator materials used in solar cell applications [21]. Other contact techniques can achieve a similar thickness range, but their multilayer capability requires a step in the material [22].

Another technique that can measure multilayer coating thickness is Spectroscopic Reflectometry (SR) [3]. SR has been implemented to measure in-situ thickness growth of other materials (SiO_2 and ZnO) in R2R semi-vacuum deposition processes [23], [24]. Nevertheless, traditional SR is also limited in scalability due to external components per inspection point, such as light sources and spectrometers.

A current state of the art in existing measurement techniques is provided in Table I. As observed, few techniques can achieve

This project was funded by the Engineering and Physical Sciences Research Council of the UK through the Intelligent Engineering Coatings for in-manufacture and in-service monitoring of critical safety products (CoatIN) (EP/T024607/1), the Future Electrical Machines Manufacturing Hub (EP/S018034/1), and the Consejo Nacional de Ciencia y Tecnología (CONACYT-México). The authors also acknowledge the support of the Royal Academy of Engineering (RAEng) and Airbus under the Research Chairs and Senior Research Fellowships scheme (RCSRF1718\5\41). For the purpose of open access, the author has applied a Creative Commons Attribution (CC BY) licence to any Author Accepted Manuscript version arising.

N.E. Sánchez-Arriaga, Divya Tiwari, Windo Hutabarat and Ashutosh Tiwari, are with the School of Mechanical, Aerospace and Civil Engineering Department, University of Sheffield, Sheffield S14DT, United Kingdom (e-mail: d.tiwari@sheffield.ac.uk)

A.C. Da Silva, is with the Department of Chemical Sciences, SSPC, the SFI Research Centre for Pharmaceuticals, Bernal Institute, University of Limerick, Limerick V94T9PX, Ireland (e-mail: arua.dasilva@ul.ie).

Adrian Leyland is an Honorary Senior Lecturer with the School of Chemical, Materials and Biological Engineering, University of Sheffield, Sheffield S13JD, United Kingdom. (e-mail:a.leyland@sheffield.ac.uk).

Manuscript received XXXX XX, 2025; revised XXXX XX, 2025.

TABLE I

STATE OF THE ART - SIMILARITIES AND DIFFERENCES OF THIN FILM CHARACTERISATION TECHNIQUES WITH POTENTIAL APPLICATION IN R2R AS COMPARED TO THE PROPOSED SOLUTION.

Technique	Thickness range (as reported)	Similarities	Differences	References
Spectroscopic Reflectometry (Proposed solution)*	125.48 - 138.82 ± 2.87 nm 201.47 - 506.03 ± 2.73 nm	Optical technique for nanometric inspection. Model-based	Multilayer capability, reduced dimensions (27.13 cm^3) Internal light source, microprocessor and spectrometer.	NA
Spectroscopic Reflectometry (SR)	0 - 400 ± 2 nm **	Same technique.	External light source, spectrometer and microprocessor. Multilayer measurements not reported.	[23], [24]
Diffractometry	115 ± 10 nm	Optical technique for nanometric inspection. Measurement range.	Fundamentals. Uses light diffraction. Suitable for patterned surfaces.	[7]
Angular Scatterometry	113-114 nm (SiO$_2$) < 1 (native oxide)	Optical technique, nanometric inspection. Depends on materials properties.	Fundamentals, angle and polarisation dependent. Sub-nanometric capability. Large dimensions.	[8], [9]
Spectroscopic Ellipsometry and Imaging Ellipsometry (SE/IE)	SE: <= 500 ± 5 nm	Both: Optical techniques, model-based. SE: Multilayer capability	Both: Fundamentals, angle and polarisation dependent Large dimensions.	[5], [6]
Hypespectral Imaging w/ SR	10 - 1050 ± 0.5 nm	Uses SR for single-point measurement.	Combines HS and SR for reconstructing 2D map. Sensor fusion approach.	[12]
Optical Coherence Tomography	max 43.5 ± 0.7 μm	Optical and model-based technique	Interferometry-based. 3D capability. Sensible to vibration. Not for the nanometric range.	[13], [14]
Focus Variation Microscopy	> 1000 ± 90 nm	Optical technique. Normal incidence. On machine capability	Fundamentals. Multiple pictures at different heights to generate a 3D profile. Large dimensions Not for thin-film multilayers.	[15]
Eddy Current	31 - 406 ± 5 nm **	Non-contact technique. Thickness range. Multilayer capability	Only for conductive materials.	[21]
Atomic Force Microscopy	0 - 1400 ± 2.9 nm	Thickness range capability	Quasi non-contact technique - Distance to sample in μm. Not for multilayer analysis	[22]

* Simultaneous multilayer measurements as reported in this paper. Can achieve 164.14 - 300.13 ± 2.57 nm on single layers. ** Material dependent.

thin film multilayer thickness analysis, and all of them remain low-scalable and high-cost solutions to accomplish the full-width measurement coverage in motion; and there are limited studies that address the thickness measurements of newer solar cell conductive polymer-type materials in such environments.

Previous work by Sánchez-Arriaga et al. presented a dimension-reduced SR device [25]; however, that work did not allow coating thickness measurements for multi-layer thin films, among multiple hardware limitations, causing variations in the angle of incidence. Additionally, there was a software development opportunity to implement the well-known curve fitting method via least squares optimisation used in SR systems for thickness measurements. Therefore, this work presents the following contributions.

- The development of a novel, highly scalable and modular single-sensor reflectometer system to measure the multilayer thin-film thickness of new flexible solar cell materials.
- A new hardware (HW) design for integrating a microprocessor (μP), a light source, a logic converter and a spectrometer sensor within a reduced-dimension enclosure, removing the angle of incidence variations.
- A unique software (SW) platform for auto-generating thin-film multilayer models and performing near real-time thickness measurements.

This work advances the current state of the art (Table I) in the area by proposing a spectroscopic reflectometry-based system that is capable of measuring multilayer thicknesses and has a reduced size of 27.13 cm^3, which is less than a quarter of the size of existing technologies. The small size of the proposed sensor system allows its installation for multilayer thickness measurements during manufacturing processes, such as R2R, where space is constrained and restricted.

To validate the capability of the newly developed sensor reflectometer, seven multilayer samples were created in a laboratory environment by modifying an existing electrode-position (ED) process [26]. The results proved the device's capability to measure the multilayer thickness of Poly(3,4-ethylenedioxythiophene): Poly sodium 4-styrene sulfatonate (PEDOT : PSS) and Indium Tin Oxide (ITO) deposited on Polyethylene Terephthalate (PET) substrates, finding a linear response of PEDOT : PSS thickness vs ED charge (thickness range: 201.47 to 506.03 ± 2.73 nm), and <7% thickness error on ITO compared to vendor specifications showing a thickness range of 125.48 to 138.82 ± 2.87 nm. Based on the results, the reflectometer design could solve the multilayer thickness measurements and width coverage in R2R manufacturing by stacking multiple reflectometers in different shapes and improving scalability and flexibility.

The remainder of this paper contains the fundamentals in section II, the methodology in sections III-IV, the experimentation, results and discussions for the proposed multilayer thickness measurements use case in section V, and the conclusions in section VI.

II. FUNDAMENTALS - OPERATION PRINCIPLE

A. Multilayer thin-film diagram

The multilayer model is based on the resultant waves and matrix methods, where the angle of incidence (θ) is assumed to be zero [27]. In this case, when two absorbing thin film layers (commonly $<1\mu$m) are stacked above each other on an absorbing substrate, light absorption is assumed per thin film layer; therefore, the extinction coefficient k must be considered in the model. The multilayer diagram for two thin films is the following (Fig. 1).

Observing Fig. 1, n_{0-3} and k_{0-3} are the refractive index and extinction coefficient of air, PEDOT : PSS, ITO and PET, respectively. E_{0-2} are reflected light rays per layer, and E_3 is the refracted light in the substrate. The positive or negative signs refer to incident/transmitted or reflected direction, Φ_x is the angle of incidence (0°), and d_1 and d_2 are the coating thicknesses of the first and second layer respectively.

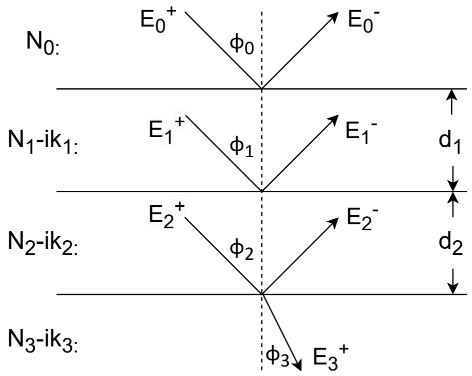

Fig. 1. Multilayer diagram: two thin films on a substrate.

B. Multilayer reflectance model of two absorbing layers and an absorbing substrate

This section shows a summarised explanation of the multilayer model [27]. The reflectance model of two absorbing layers on an absorbing substrate is defined by Equation (1),

$$R_2(d_2, t_{12}, u_{12}, p_{12}, q_{12}, n_3, k_3) = (t_{13}^2 + u_{13}^2)/(p_{13}^2 + q_{13}^2), \tag{1}$$

where R_2 is the reflectance of two absorbing layers and an absorbing substrate; t_{13}, u_{13}, p_{13}, and q_{13} are complex matrix elements containing the effects of both layers (d_1 and d_2) and the substrate, their respective refractive indexes n_1, n_2, n_3 and their extinction coefficients (k's) per wavelength (λ). For example,

$$p_{13} = p_{12}p_3 - q_{12}q_3 + r_{12}t_3 - s_{12}u_3, \tag{2}$$

where,

$$q_{12} = q_2 + h_1 t_2 + g_1 u_2, \tag{3}$$

and,

$$q_2 = e^{\alpha_1 sin\gamma_1}. \tag{4}$$

Then, the phase terms in radians are defined as

$$\alpha_1 = 2\pi k_1 d_1/\lambda, \tag{5}$$

$$\lambda_1 = 2\pi n_1 d_1/\lambda, \tag{6}$$

where k_1, d_1, and n_1 ($n_1 \equiv n_1$-ik_1) are the extinction coefficient, the thickness and the complex refractive index of the first layer, respectively, and λ is the wavelength under study. The rest of the complex refractive index of each layer remains embedded within the matrix multilayer equations. The full multilayer equations are extensive. The full derivation can be found in [27].

Equation 1 can model a reflectance curve when analysing a bandwidth of wavelengths (λ) (see Fig. 9), then the modelled reflectance curve can be compared with a measured reflectance curve and evaluate the measurement accuracy with cost functions such as the Root Meas Squared Error (RMSE); or could be used for indirect thickness measurements with least square optimisation methods.

C. Least squares optimisation

The thin film thickness values are estimated and extracted from mathematical models using non-linear least squares optimisation algorithms in SR systems [28]. These methods are iterative procedures that minimise the residuals/errors (r_i) between measured and modelled values by finding their derivatives following the L2 norm [29]. For example, following the Gauss method, given a function $g(x)$ such as Equation (1) and measured values y_i where $i = 1 : m$ is the ith observation, the errors (residuals) between the measured values and the function output can be expressed as:

$$r_i(x) = y_i - g(x) \quad with \quad i = 1 : m, \tag{7}$$

this becomes a vector $r(x) = [r_1(x), ..., r_m(x)]^T$. The challenge of the non-linear squared optimisation algorithms is to find the real values of x that globally minimise the sum of the squared residuals, where an iterative process is performed to calculate the step δ, and update for the new value $x_{k_{new}}$ [29], [30], therefore:

$$x_{(new)} = x + \delta. \tag{8}$$

This process is repeated until the optimal values are found to minimise the errors [28]–[30]. In practice, the x values in Equation 7 could be any, such as d_2 in Equation 1 or others, depending on the chosen $g(x)$ function to optimise. In this case, the least squares optimisation methods help find the best parameters that decrease the errors (r_i); thus, these are considered the estimated desired measurements.

Although it is widely known that the least squares optimisation methods present local minima issues during operation [10], they are known for being precise and easy to apply in practice. The trust region methods are the most popular in SR, where the Gauss method serves as a baseline for others [31] [32]. The dogbox algorithm is an improved method of Powell's Dogleg algorithm, which can work with bounds in a rectangular-shaped region [32]. The literature has proven that the Dogleg algorithm outperforms LM on speed and computational costs [30]; additionally, the Dogbox method has not been reported in SR applications; consequently, it will be explored in this work by applying it with the Python scipy curve_fit function.

III. HARDWARE DEVELOPMENT AND TEST SETUP

A. Component selection methodology

Finding the appropriate components for designing a prototype is complex during the development phase because of several factors, such as the variety in the market, the component specifications and the desired system functionality. The following features were prioritised when choosing the components for developing the SR system: low cost, reduced dimensions, modularity for large-area coverage, and potential for IoT implementation when evaluating the μP. Any other feature was evaluated per component, e.g. the visible spectrum was prioritised when choosing a sensor and a light source. Therefore, a modified weighted matrix was created, inspired by [33], [34], to help the design process. See Table II.

TABLE II
COMPONENT SELECTION WEIGHTS AND COLOUR CODES

Weights				
5	4	3	2	1

Note: 5: More desired, 1: Less desired

The weights in Table II were assigned and summed per feature when evaluating each one of the components in Table III, IV and V.

Sensor selection

The Hamamatsu spectrometer family was selected due to its small dimensions and low-cost product offering. The selection of the best spectrometer sensor to comply with the research objectives was conducted, as shown in Table III.

TABLE III
WEIGHTED MATRIX - SPECTROMETER SENSOR SELECTION

Model	Type	Spectrum range (nm)	Spectral resolution (nm)	S/N (ratio)	Size (mm)	Cost (€)	Summed weight
C12666MA	Wide dynamic range	340 780	12	5300:1	20.1x12.5x10.1	416.94	26
C12880MA	High sensitivity	340 850	12	330:1	20.1x12.5x10.1	418.06	24
C14384MA	Ultra compact	640 1050	17	330:1	11.5x4x3.1	426.46	23
C11009MA	Wide dynamic range	340 780	6	5600:1	28x28x28	1665.6	22
C11010MA	Wide dynamic range	640 1050	6.5	5600:1	35x28x20	1666.8	20
C11708MA	near IR	640 1050	15	5300:1	27.6x16.8x13	713.24	19

As observed, the sensor C12666MA was selected to conduct the design of the SR device. This sensor has the advantage of being the most compact spectrometer with visible spectrum capabilities, offering a wide dynamic range and a better signal-to-noise ratio compared to the next best spectrometer, the C12880MA, which easily saturates due to its high sensitivity [25]. Although the C12666MA is not the best spectrometer in terms of the spectral resolution per pixel, its dimensions and cost made it a suitable sensor for this work.

Light source selection

The selection of the best light source was conducted as shown in Table IV.

The white light LED 713-3983 (manufacturing PN: NSPL500DS) was selected for research purposes. LEDs have the advantage of being low-cost and having small dimensions compared to commercial light sources used in SR systems. However, their use is restricted for spectroscopy because they are limited to the visible spectrum (450 nm to 700nm) and show a high peak in the blue zone of the spectrum, affecting their flatness [28]. The LED MBB1D1 was discarded due to safety reasons and overheating (1800mW). The remaining light sources are commonly used in SR systems; however, their dimensions and costs were a limiting factor for this work.

TABLE IV
WEIGHTED MATRIX - LIGHT SOURCE SELECTION

Product	Spectrum range (nm)	Light source type	Power (mW)	Size (mm)	Spectrum flatness (%)	Fwd Volt (dc)	Cost (€)	Summed Weight
713-3983	450 750	LED	105	θ:5.3	90	3.2	<1	29
MBB1D1	470 850	LED	1800	θ:22	99	3.6	411.8	25
HAL-S-Mini	360 2500	W/HAL	5.97*	150x78 x37	99	12	1856	25
DHc	200 2500	HAL DEUT	0.007*	175x110 x44	95	12	1310.8	24
DH-S-BAL	215 2500	HAL DEUT	0.193*	315x165 x140	85	n/a	2484.7	19

Note: *Power output of fibre optic probes. HAL: Halogen; DEUT: Deuterium. The spectrum flatness is the ratio of the geometric mean divided by the arithmetic mean [36], [37]

Microprocessor board selection

A similar exercise was conducted to select the best μP. Table V shows the weighted matrix for the μP selection.

TABLE V
WEIGHTED MATRIX - MICROPROCESSOR BOARD SELECTION

Brand	Model	Max ADC	DIM LxW (mm)	Clock Speed (Mhz)	Input Voltage (Vdc)	USB Type	Wifi	BT	Cost (€)	OPAMP	Summed Weight
Arduino	Uno*	10	68.6 x 53.4	16	7-12	Micro	N	N	27.8	N	N/A
Arduino	Nano 33IoT	12	45 x 18	48	5-21	Micro	Y	Y	22.3	N	40
Arduino	Nano RP2040	12	45 x 18	133	1.8-5.5	Micro	Y	Y	30.6	N	37
Particle	Photon (v021)	12	37 x 20.3	120	3.6-5.5	Micro	Y	Y	22	N	37
Raspberry Pi	Pico W	12	21 x 10.5	133	5	Micro	Y	N	7	N	36
Adafruit	Feather Huzzah32	12	51 x 23	240	3.6-5.5	Micro	Y	Y	23.1	N	36
STM	Nucleo L432KC	16	48 x 18	24	5	Micro	N	N	11.7	Y	35
Seed Studio	Xiaio ESP32C3	12	21 x 17.5	160	5	C	Y	Y	5.8	N	35
Arduino	Nano 33BLE	12	45 x 18	64	5-21	Micro	N	Y	24.4	N	34
Arduino	Nano 33 BLE S	12	45 x 18	64	5-21	Micro	N	Y	37.6	N	33

Note: *Used as a baseline for selecting the μP specifications [38]. DIM: Dimensions, OPAMP: Operational Amplifier, BT: Bluetooth.

The potential for wireless connectivity was one of the desired features to support the inspection flexibility needs for R2R manufacturing. In this regard, several boards in the table showed a type of wireless connectivity option. However, it was discovered that the Nucleo L432KC was the only board that showed an operational amplifier (OPAMP) as an analogue input to the internal Analog-to-Digital (ADC) converter of the μP. According to the specification sheet of the Hamamatsu sensors, this is an optional requirement to prevent sensor overheating during video signal acquisition. Therefore, the sensor needs were prioritised over the rest of the features offered by other μP boards. Additionally, the Nucleo L432KC has a faster clock speed than the baseline Arduino Uno and the potential to increase the ADC resolution up to 16-bit with oversampling in the future.

B. Reflectometer block diagram, circuit and materials

Fig. 2 shows the reflectometer block diagram.

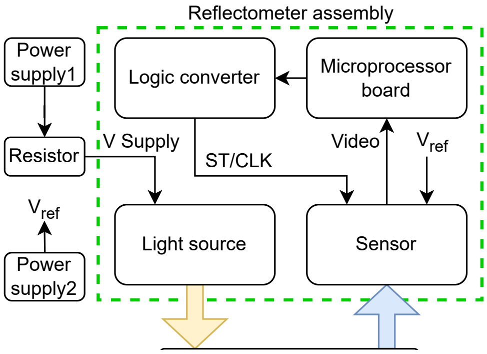

Fig. 2. Reflectometer design - Block diagram.

As shown in Fig. 2, the μP Nucleo L432KC, the logic converter TXS0108E, the LED NSPL500DS and the sensor C12666MA are integrated into the assembly. A variable resistor 67WR10KLF and a power supply D03232 are connected externally to the LED. Additionally, another power supply, D03232 was used to provide a reference voltage of 2.9 V to the VDDA (AREF) pin of the μP. These features required the precise design of 3D parts and cabling arrangements, which are discussed in the following section.

C. Reflectometer assembly: Instructions

Fig. 3 shows the board subassembly process, including the μP and the logic converter.

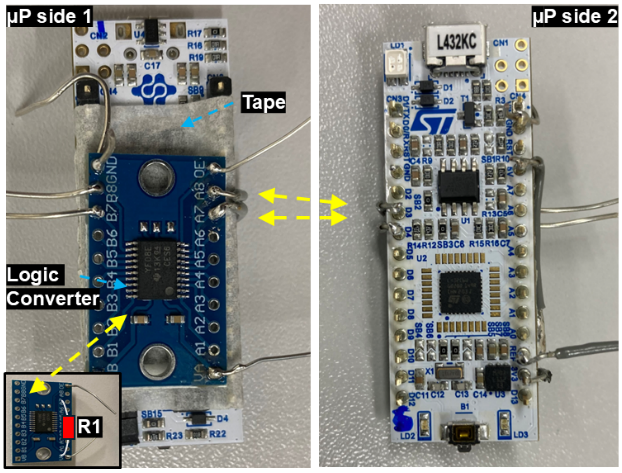

Fig. 3. Boards sub-assy (μP and logic converter). Left corner inset: R1 installed on the back of the logic converter.

As observed, an insulator tape was installed between boards for safety purposes to avoid short circuits; then, the soldered connections will hold the logic converter in its place. Fig. 4 shows the reflectometer sub-assembly.

Fig. 4a shows an IC socket A14-LC-TT with 6cm-long cables soldered on each pin as specified. The IC socket was used as an interface to avoid damaging the sensor during the soldering process. Fig. 4b shows the board sub-assy with the sensor. The final reflectometer assembly is completed, as shown in Fig. 5.

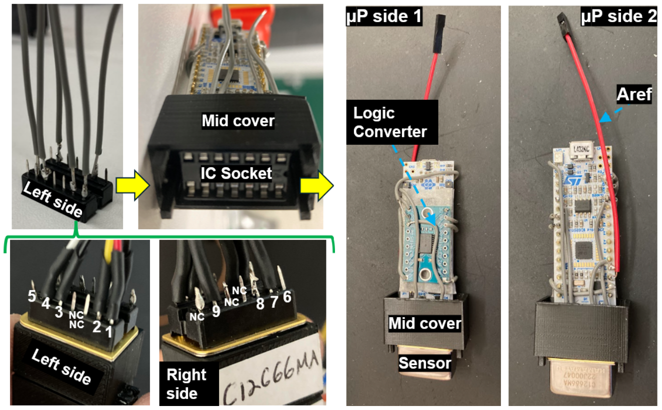

(a) (b)

Fig. 4. Reflectometer sub-assembly. (a) IC socket cabling and sensor pinout. (b) Board sub-assy with sensor.

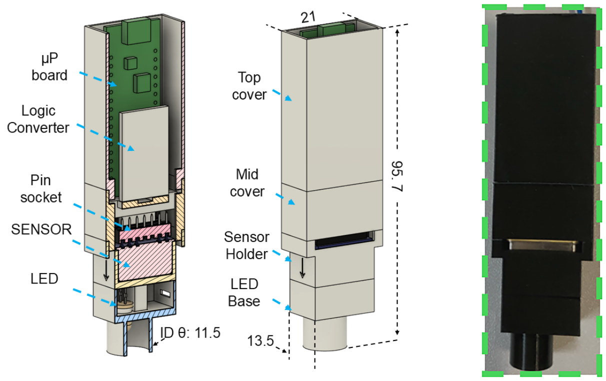

(a) (b)

Fig. 5. Single-sensor reflectometer assembly (a) 3D view and cross section showing the μP and logic converter addition (b) Final single-sensor reflectometer assembly. All dimensions in mm.

Fig. 5a shows the 3D-view of the single-sensor reflectometer and the position of the internal and external components, and 5b shows the final single-sensor reflectometer assembly.

D. Test Setup

Additional components were developed to complete the test setup. See Fig. 6.

Fig. 6a shows the setup 3D view. The reflectometer holder and the reflectometer holder lock were designed to keep the reflectometer in the test position as close to normal incidence to the coated sample; a second reflectometer holder was used as a sample holder to place the sample under the reflectometer inspection position.

Fig. 6b shows the physical test setup where a Dinolite microscope stand (RK-10A) held the developed reflectometer in the test position. The distance from the sample to the tip of the reflectometer was 2 mm measured manually with the integrated adjustment of the RK10A, and the light intensity was set to 944 Lux measured with a Dr Meter Luxometer (LX1330B). The microscope stand and the Thorlabs base

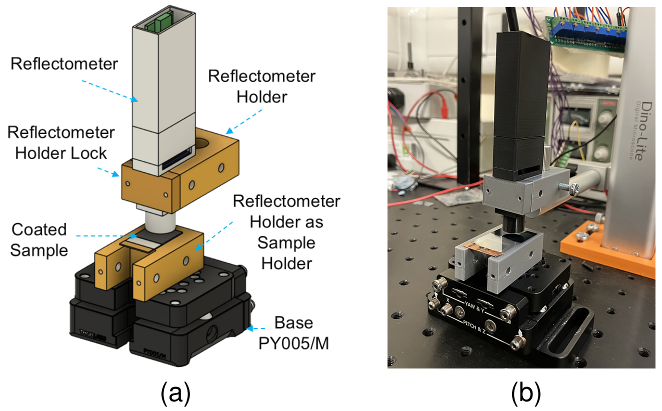

Fig. 6. Test setup (a) 3D view of the new reflectometer test setup (b) Physical reflectometer and test setup parts. Thorlabs base PY005/M 3D view reproduced with permission.

PY005/M were attached to a Thorlabs aluminium breadboard Mb1445/M.

E. Methodology for reflectance measurements and calibration

The reflectance measurements per pixel of a coated substrate (R_c) are a ratio expressed as:

$$R_c = (I_c - I_d)/(I_u - I_d), \tag{9}$$

where the dark noise intensity (I_d) of a spectrometer sensor is subtracted from the reflected intensity of an uncoated reference (I_u) and a coated (I_c) substrate; Figure 7 exemplifies this process in four steps where the first two are the calibration steps.

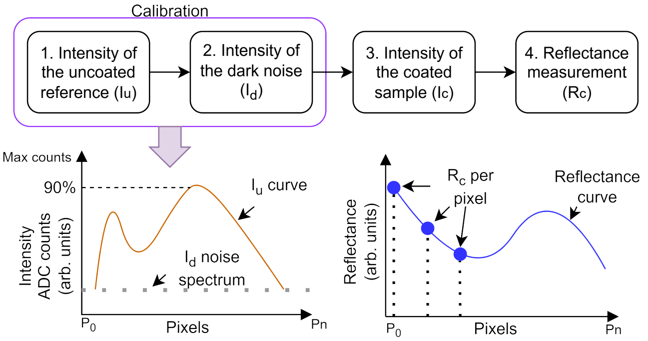

Fig. 7. Measurement and calibration process in SR. The curves were made manually for explanation purposes.

i) Intensity of the uncoated reference. The reflected spectrum of an uncoated reference must be measured. The μP integration time and light intensity must be adjusted so the peak of the reflected spectrum reaches 90% of the available analogue-to-digital converter (ADC) (see Figure 7 bottom left) [17]. Using an uncoated reference standard is recommended for reflectance calibration purposes; however, using an uncoated sample with known refractive index can be used when a reference standard for the material is not available [23], [24], [28].

ii) Intensity of the dark noise. The light source must be turned off to capture the dark noise intensity spectrum. An average of a maximum of one hundred intensity measurements of the uncoated reference (I$_u$) and dark noise (I$_d$) is recommended for calibration purposes [41], [42]; however, this is open to user needs. Section V shows the practical approach to achieving the results in this work.

iii) Intensity of the coated sample. After calibration, the light must be turned on again, and a coated sample must be placed in the test position to capture the intensity.

iv) Reflectance measurement. The reflectance measurement is calculated from Equation (9). Observing the bottom right of Figure 7, each pixel shows a corresponding reflectance point (R_c). Consequently, a reflectance curve is formed across the spectrometer sensor pixels. Each sensor pixel is preset with a wavelength by the vendor. The measured reflectance curve can be used for comparison purposes with the model as explained in section II-B, and the thickness measurements can be performed by fitting a curve within the measured reflectance curve as explained in section II-C.

IV. SOFTWARE DEVELOPMENT

This research presents an automated multi-layer reflectance model generator script, which enables real-time thickness measurements using least squares optimisation with the curve_fit SciPy package. The software development scripts were designed to comply with the fundamentals in Section II.

A. Reflectance script

Fig. 8 shows the block diagram where the reflectance, calibration and refractive index scripts were developed using Python version 3.10.

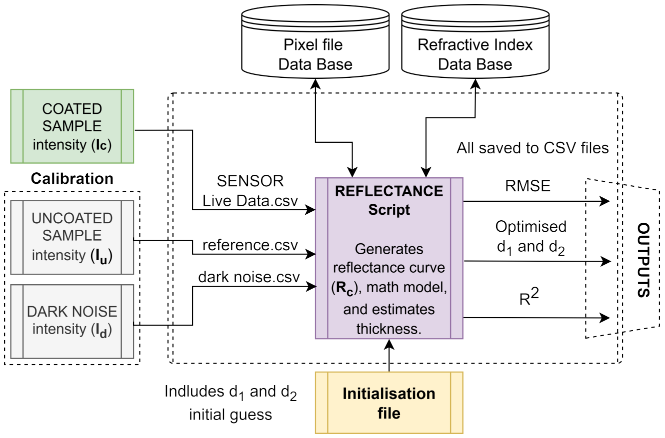

Fig. 8. Reflectance script top-level block diagram.

As observed, the reflectance script performs three major tasks: (i) it generates a reflectance curve by loading the calibration files and read live data from the sensor, (ii) it autogenerates a mathematical model for comparison purposes and calculates the RMSE, and (iii) it estimates the thickness based on the non-linear least squares method.

i) Reflectance curve generation. This script was designed to comply with Section III-E. As observed, the script loads the calibration pre-generated files by two scripts: the uncoated reference (I_u) and dark noise (I_d). Then, it calculates (R_c) by reading the live intensity data of the coated sample (I_c) as defined in Equation (9). Section V expands on the experimental approach in this paper.

ii) Multilayer model generation. This is enabled by reading the initialisation file containing the expected thickness per layer, the type of materials under study and the angle of incidence. Then, the reflectance script reads the Pixel File to get the sensor pixel wavelengths and generate the model based on Equation (1). Once the model and the reflectance measurements are ready, the Root Mean Squared Error (RMSE) is calculated.

iii) Thickness estimation. The final step is the thickness estimation using least squares optimisation as described in Section II-C. The reflectance script reads the initial guess of d_1 and d_2 from the initialisation file; then, these values are input to the Python SciPy curve_fit function (method: Dogbox); then, curve_fit returns the optimised d_1 and d_2. This process fits a curve within the live sensor measurements, which is done by using the new optimised thickness values of d_1 and d_2 in the model stated in Equation (1). Once the fitted reflectance line is generated, the R^2 is calculated using the Scipy r2_score function.

B. *Reflectance script validation*

Fig. 9 compares the theoretical multilayer model (PET / ITO : PEDOT : PSS) with the Python-generated reflectance model and with the model generated by the Filmetrics calculator [39].

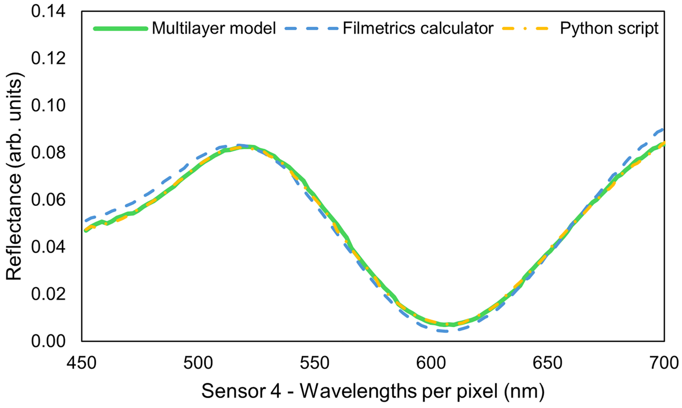

Fig. 9. Reflectance model comparison at randomly selected thickness values: d_1:485nm and d_2:114nm. The Python model was generated synthetically for the script validation purposes.

Regarding the Filmetrics-generated model, the PEDOT : PSS refractive index is not available in the Filmetrics calculator database; however, the calculator allows the refractive index estimation of a material by adding dispersion and defining a bandwidth around a defined wavelength of 632.8 nm. The refractive index of PEDOT : PSS was found in [40] and used to generate the estimated reflectance curve with the Filmetrics calculator and perform the comparison. All the reflectance curves were similar, demonstrating that the Python script calculates them accurately. Section V shows the experimental results.

V. USE CASE: MEASURING THE THICKNESS OF MULTILAYER FILMS OF AN ELECTRODEPOSITED SAMPLE.

A. *Calibration settings*

The reflectometer physical position with respect to the sample was described in Figure 6b. The calibration steps were performed as described in section III-E. Thirty measurements were selected as a baseline to keep the measurement time during calibration below two seconds per spectrum measurement. Increasing the number of averages would increase the calibration time beyond 2.5 minutes, which is not practical for our demonstration purposes. Additionally, the integration time was set to 0.2 seconds and the light intensity to 944 Lux as mentioned in section III-D.

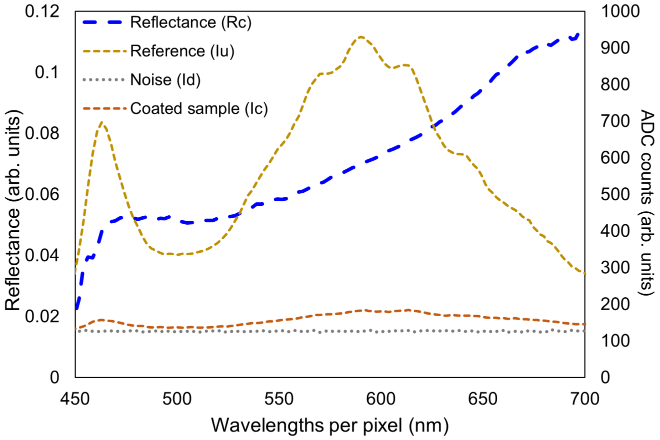

Fig. 10. Calibration graph of Sample E1 (Appendix A) showing the uncoated reference and noise spectrums; and the live measured reflectance

As observed in the calibration graph Figure 10, a reflectance curve (in dotted blue lines) was generated after following the calibration steps. This curve can be compared to a modelled curve using the RMSE; then, another curve can be fitted in it using the least squares optimisation to estimate the thickness measurement. See section II for fundamentals and section IV for the description of the reflectance script that enables this process.

B. *Experimental Results and Discussions*

B.1 *Python screen results - single measurement*

The new reflectometer multilayer measurement capability was tested on seven PET / ITO / PEDOT : PSS samples created in the lab described in the Appendix A. Figure 11 shows the Python script output screen.

Figure 11 shows the Python screen and the reflectance curves of sample E1 (modelled, measured and fitted-optimised), where the experimental model is automatically generated by the Python script and is based on the same theoretical model in Equation (1). The bottom of the screen shows the system outputs RMSE, R^2 and measured (optimised) thicknesses d_1 and d_2. The “Exp” (expected) thickness values are the initial best guess set in the initialisation file as explained in Section IV. The following section shows the full data set analysis with an increased sample size for each ED sample.

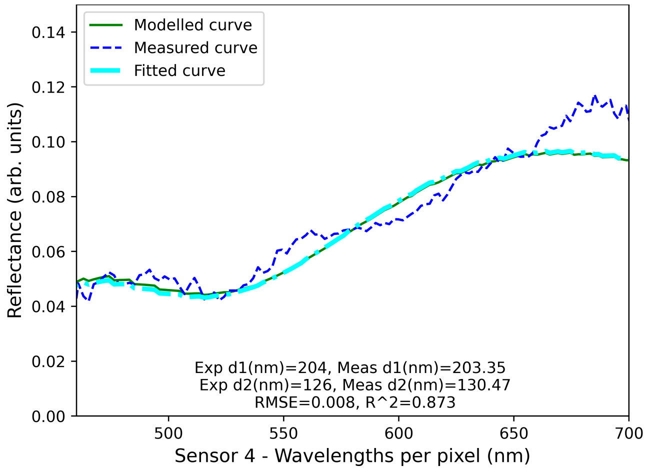

Fig. 11. Sample E1 - Python screen output of a single measurement. (Note: Exp: Expected; Meas: Measured)

B.2 Full data set analysis

Fig. 12 shows the averaged thickness measurements of d_1 and d_2 vs ED charge of the seven electrodeposited samples.

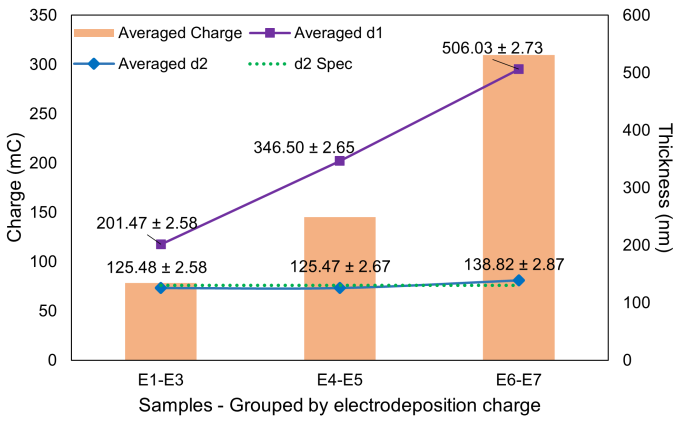

Fig. 12. Thickness response (d_1 and d_2) vs ED charge. The samples were grouped by ED charge, and the d_1 and d_2 data were measured simultaneously and averaged after >130 measurements per sample. The data points are the mean ± Uncertainty @ 95% confidence interval. Orange block: Averaged charge. Purple line: Averaged d_1. Light blue line: d_2. Red marker: d_2 spec: 130nm

As shown, d_1 increases with ED charge, showing a linear response vs charge (see Appendix A for ED charge information). This finding is promising, suggesting that the method presented in this work could measure PEDOT : PSS thickness up to 506.03 ± 2.73 nm @ 95% confidence level. Additionally, d_2 remains within <7% error compared to the vendor specification in all samples (vendor spec PN:639303-5EA is 130nm), showing a max thickness of 138.82 ± 2.87 nm @ 95% confidence level. Table VI shows a summary of the thickness measurements data. As observed, the PEDOT:PSS thickness (d_1) changes with charge, while the ITO layer (d_2) remains close to the specified value of 130 nm, as expected. The following section explains the uncertainty calculation.

TABLE VI
SUMMARY OF THICKNESS MEASUREMENTS RESULTS OBTAINED FROM SEVEN SAMPLES E1 → E7

Sample	d_1 (nm)	σ (nm)	u_c (nm)	U @ 95% (nm)	d_2 (nm)	d_2 spec (nm)	d_2 Error (%)	σ (nm)	u_c (nm)	U @ 95% (nm)
E6-E7	506.03	5.42	1.36	2.73	138.82	130	6.78	7.41	1.43	2.87
E4-E5	346.50	3.88	1.33	2.65	125.47		3.48	4.36	1.34	2.67
E1-E3	201.47	1.49	1.29	2.58	125.48		3.47	1.40	1.29	2.58

All the data in this table is averaged. PET:ITO sheet PN:639303-5EA. σ: standard deviation; u_c: combined uncertainty and U: expanded uncertainty. Data set [43].

B.3 Uncertainty calculation

The uncertainty was calculated as described by the National Physics Laboratory (NPL), considering the Type A and Type B uncertainties at 95% confidence interval level using a k factor: 2 [46]. Therefore, the Type A uncertainty was calculated as $u = \sigma/\sqrt{(n)}$ where n is the sample size; and then the combined uncertainty as $u_c = \sqrt{(u^2_{TypeA} + u^2_{TypeB})}$. In this case, the Type B uncertainty was defined by the data sheets of the spectrometer, where the following uncertainties were considered [47]: spectrometer wavelength reproducibility (max: ± 0.8 nm); wavelength temperature dependence (max: ± 0.08 nm) and an additional uncertainty due to mechanical positioning (± 1 nm). Finally, the expanded uncertainty (U) was calculated as $U = ku_c$ with a coverage factor of k = 2 for a 95% confidence interval level. All the tests were performed under a controlled room temperature of 23°C. The following section explains the RMSE and R^2 analysis.

B.4 RMSE and R^2 analysis

The RMSE remains low in all the samples (< 0.015), a good indicator of comparison between the modelled and the measured reflectance curves. Finally, the R^2 shows promising values of GoF on optimising the thickness by fitting a curve within the measured values. The R^2 values (averaged per group) were 0.79 for samples E1 - E3, 0.82 for samples E4 - E5, and 0.75 for samples E6 - E7. Fig. 13 shows the reflectance curves of the experiment. The reflectance values per chart were averaged to facilitate the visual analysis.

As observed, the measured reflectance curves are close to their models, which explains why the RMSE is getting low values <0.015; however, the R^2 was close to 0.8 for all the samples. According to industry experts, an R^2>0.95 must be expected as a good fit indicator. The samples E1-E5 show similar reflectance curve shapes compared to the models. However, the reflectance curves of E6-E7 start deviating from their models. This deviation could be explained by an important feature of the coatings, the surface roughness, which explains how smooth a surface is compared to others.

Table VII shows the surface roughness metric (Ra) measured with an Alicona Focus x Microscope, where two aluminium polished mirror-finish samples were used for comparison.

As observed, the ED samples presented more variation; all presented higher surface roughness than aluminium mirror-

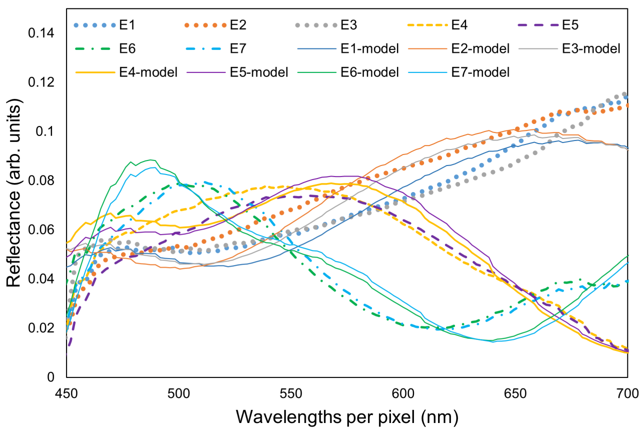

Fig. 13. Reflectance curves of samples E1 to E7. All data was averaged. Dashed lines: Measurements. Solid lines: Models

TABLE VII
SURFACE ROUGHNESS COMPARISON USING ALICONA FOCUS X MICROSCOPE

Sample ID	Ra (μm)	Sample ID	Ra (μm)	Sample ID	Ra (μm)
E1	0.53	E4	0.38	E7	0.314
E2	0.416	E5	0.735	Al_0.25	0.133
E3	0.207	E6	0.296	AL_0.05	0.158

All units centred, Ra measurements within 1 μm linear inspection zone.

finished samples. Other sources of variation must also be considered.

- **Roughness effects in model**. Equation 1 works well assuming ideal conditions; however, roughness must be considered in the model to improve accuracy [48]. Future work will explore the effects of roughness on the reflectance model by implementing known roughness correction models, understanding their advantages and limitations with conductive polymer materials as presented in this work and improving them with innovative approaches.
- **Reference**. An uncoated PET sample with 150 μm thickness from Plasfilms was used as a reference for calibration purposes. The sample differs from the ITO-precoated PET films purchased from Merck. The ITO-coated PET from Merck is 127 μm, whilst the Plasfilms PET sheet has a 150 μm thickness. Merck does not sell an uncoated PET version. Therefore, having the same uncoated PET as provided by Merck could significantly improve the reflectance curve shape and the R^2 metric.
- **Electrodeposition process**. As observed, the ED process can not ensure a flat, homogeneous surface, causing roughness variations and potentially affecting the thickness measurements.
- **3D printed part variation**. The sample holder was printed in-house in an i3-MK3 3D printer, having 0.2 mm variation per specifications; therefore, misalignments could affect the reflected intensity.
- **Intensity offset of the uncoated samples** Due to an offset presented in the coated samples, the integration time was set to 200 units (0.2 s) first when measuring the reflected intensity of the uncoated samples; however, the integration time was modified to 25 units (0.025 s) when measuring the coated samples E1-E5, then to 50 units (0.05 s) for E6-E7 for experimental purposes. The offset was constant, without drift over time, and kept the same reflectance curve in the VIS spectrum; therefore, following the National Physical Laboratory (NPL) practices to fix offsets [44].
- **Reflectance model vs measurement mismatch.** Selecting the initial best-guess of thickness value could lead to measurement inaccuracies and increased errors due to model and measurement mismatch. Therefore, we implemented the RMSE and R^2 simultaneously to improve accuracy and reduce the thickness errors to the lowest possible, which is not a normal practice in the industry. Reflectance industry leaders only use the R^2 as a GoF indicator [41], [42]. Others are implementing machine learning to improve the initial thickness estimate and improve accuracy [45]. Future developments will explore this approach to reduce uncertainty in thickness measurements.

The sources of variation added complexity when measuring the thickness values. Once the samples were placed into the test position, the SW found the optimised thicknesses of d_1 and d_2. Any other source of variation could be related to mechanical and optical effects due to the in-house laboratory setup or light source stability.

Since this work is focused on multilayer measurements of specialised off-the-shelf compounds used in new solar cell generation materials, it was not possible to find a commercial PEDOT : PSS / ITO / PET standard sample to compare the measurements; however, single-layer measurements were also made available by enabling the single-layer model [17], [19], and performing optimisation as presented in this paper, showing that our device could measure coating thickness with $\leq$ than 1.51% error compared to a commercial Filmetrics-F20 reflectometer. Table VIII shows the comparison.

TABLE VIII
SINGLE-LAYER MEASUREMENTS COMPARISON VS COMMERCIAL REFLECTOMETER

			Measurements		
Sample	SiO_2 vendor spec (nm)	Vendor tolerance (%)	Filmetrics F20 (nm)	Our system (nm)	Error (%)
1	300	20	304.74 ± 2	300.13 ± 2.57	1.51
2	300	20	286.86 ± 2	283.58 ± 2.57	1.14
3	150	10	162.32 ± 2	164.14 ± 2.57	1.12

Our system sample size was 300 per sample over two days for repeatability purposes. A Filmetrics TS-SiO2-6-Multi Standard was used for calibration. The F20 sample size was 30 per sample at the Imperial College of London.

As observed, our reflectometer was precise compared to a commercial reflectometer. Future work will address the mentioned sources of variation and limitations to deliver the full potential of SR in-process inspection in R2R manufacturing.

VI. CONCLUSIONS

This work presented a unique in-house developed reflectometer with thin-film multilayer measurement capability for flexible electronics applications. Key findings were the reflectometer's capability to characterise a layer of Indium Tin Oxide with a thickness ranging from 125.48 to 138.82 ± 2.87 nm which represents an error below 7% compared to vendor specifications (130 nm); and the linear thickness response of Poly(3,4-ethylenedioxythiophene) : Poly sodium 4-styrene sulfonate vs electrodeposition charge, ranging between 201.47 to 506.03 ± 2.73 nm, giving certainty to our measurements. This work advances the current state of the art in the area by proposing a spectroscopic reflectometry-based system that is capable of measuring multilayer thicknesses and has a reduced size of 27.13 cm^3, which is less than a quarter of the size of existing technologies. The small size of the proposed sensor system allows its installation for multilayer thickness measurements during manufacturing processes like R2R, where space is constrained and restricted. Additionally, the simultaneous measurement of PEDOT:PSS and ITO is a promising feature for new solar cell research, development and manufacturing.

Future work implies stacking multiple sensors to extend the thickness measurements across the width of a coated substrate; additionally, implementing innovative machine learning methods is a potential research path to follow to improve the fitting methods and the accuracy of the thickness measurements.

CONFLICT OF INTEREST

The following authors are commercially interested in the reflectometer design under the submitted patent application number GB2417203.3: Néstor Eduardo Sánchez-Arriaga, Divya Tiwari, Windo Hutabarat, Adrian Leyland and Ashutosh Tiwari.

ACKNOWLEDGMENT

The authors thank Thorlabs Inc. for authorising the PY005/M 3D view, Dr. John Walker from Plasfilms for donating PET samples and The Henry Royce Institute at the Imperial College of London for the funding and access to the Filmetrics F20 reflectometer.

APPENDIX A
SAMPLE CREATION PROCEDURE

As mentioned, an ED process was modified from previously reported work [49], [50]. Regarding materials, the PSS (PN:243051-100G) and a pack of ITO-coated PET (PN: 639303-5EA) were obtained from Merck. Additionally, a bottle of 3,4-Ethylenedioxythiophene (EDOT) monomers (PN: 10-F047796) was purchased from Fluorochem.

Fig. 14 shows the process of creating electrodeposited samples.

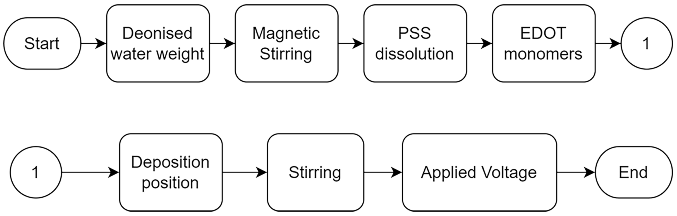

Fig. 14. Electrodeposition process- sample creation

The new process starts by weighing 23.4 g of deionised water in a 50 mL beaker. Subsequently, a magnet is added, and the magnetic stirring is kept at 600 rpm. Then, 86.21mg of PSS were dissolved in the solution for a 0.02 mol/L concentration. Finally, 26.77 μL of EDOT monomers were dissolved in the same beaker and stirred for 20 min to obtain the EDOT concentration of 0.01mol/L. An ITO-coated PET sheet was cut into seven 2.5 cm x 1.5 cm rectangles, and the target coated area was 1.5 cm x 1.5 cm. Then, segments of copper tape were attached to one of the short sides to improve connection and facilitate the sample positioning to perform the PEDOT : PSS ED. Finally, the prepared ITO-coated PET flexible electrode was positioned as a working electrode, a platinum coil as a counter electrode and a commercially available Ag/AgCl/KCl 3M (BASi) as a reference electrode. Fig. 15 shows the electrodeposition setup.

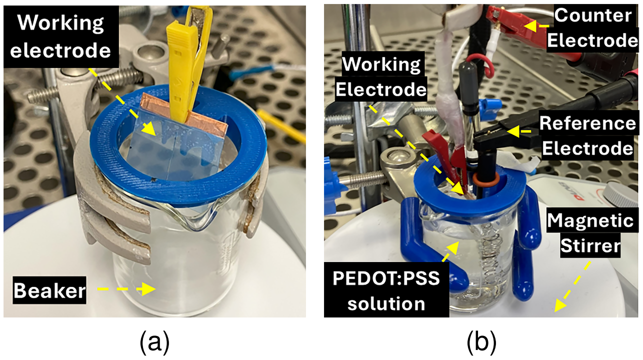

Fig. 15. ED three-electrode setup. (a) Working electrode sample (prepared ITO-coated PET flexible electrode) with copper tape (b) Sample in position for ED.

Once the sample was placed into the electrodeposition position 15b, the solution was stirred at 200 rpms. Then, using the VersaStudio SW in chronoamperometry mode, a constant 1.5 V was applied for different intervals per sample, coating the ITO surface with a layer of PEDOT : PSS. Fig. 16 shows the resulting PET / ITO / PEDOT : PSS samples.

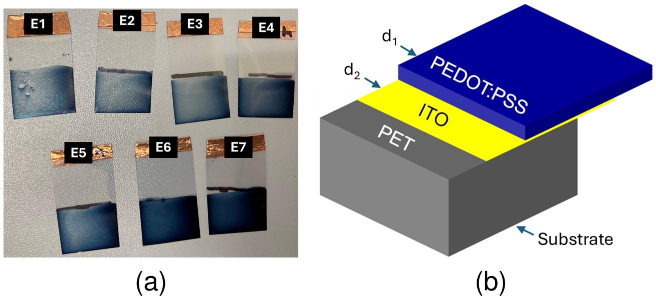

Fig. 16. Electrodeposited samples (a) Electrodes 1 - 7. (b) Sample diagram where d_1 is the thickness of layer 1, and d_2 is the thickness of layer 2.

As observed, seven samples were made using ED following the described procedure. Table IX shows the electrodeposition charge, time and current per sample; the deposition rate can be deduced, resulting in $J = 1$ mA/cm^2.

TABLE IX
ELECTRODEPOSITION TIME AND CHARGE PER SAMPLE

Sample	ED time (s)	Current (mA)	Charge (mC)
E6 - E7	120	2.58	309.76
E4 - E5	60	2.42	145.14
E1 - E3	30	2.60	78.19

Results were averaged per sample group.

REFERENCES

[1] International Renewable Energy Agency (IRENA), “Global energy transformation: A roadmap to 2050”, Abu Dhabi, 2019. ISBN: 978-92-9260-059-4.

[2] C. Martin, Q. Zhao, A. Patel, E. V. Morquecho, D. Chen, and W. Li, “A review of advanced roll-to-roll manufacturing: System Modeling and Control,” Journal of Manufacturing Science and Engineering, vol. 147, no. 4, Nov. 2024, doi: https://doi.org/10.1115/1.4067053.

[3] K. Maize, Y. Mi, M. Cakmak, and A. Shakouri, “Real-time metrology for roll-to-roll and advanced inline manufacturing: A review,” Advanced Materials Technologies, vol. 8, Nov. 2022.

[4] S. Venkatesan, M. A. Cullinan, and M. Baldea, “Recent advances in continuous nanomanufacturing: focus on machine learning-driven process control,” Reviews in Chemical Engineering, Dec. 2024, doi: https://doi.org/10.1515/revce-2024-0029.

[5] F. Münch, B. Hauer, I. Breunig, and D. Carl, “Multi-Angle averaging approach for measuring the coating thickness on thin transparent polymer films,” Applied Spectroscopy, May 2025, doi: 10.1177/00037028251334152.

[6] F. Bammer and F. Huemer, “Inline thickness measurement with imaging ellipsometry,” Photonics and Education in Measurement Science 2019, p. 36, Sep. 2019, doi: https://doi.org/10.1117/12.2531940.

[7] G. L. Whitworth, A. Francone, C. M. Sotomayor-Torres, and N. Kehagias, “Real-time Optical Dimensional Metrology via Diffractometry for Nanofabrication,” Scientific Reports, vol. 10, no. 1, Mar. 2020, doi: https://doi.org/10.1038/s41598-020-61975-3.

[8] J. J. Faria-Briceno et al., “Optical angular scatterometry: In-line metrology approach for roll-to-roll and nanoimprint fabrication,” Journal of Vacuum Science & Technology B Nanotechnology and Microelectronics Materials Processing Measurement and Phenomena, vol. 37, no. 5, Sep. 2019, doi: https://doi.org/10.1116/1.5119707.

[9] J. J. Faria-Briceno, Vineeth Sasidharan, A. Neumann, S. Singhal, S. V. Sreenivasan, and Steven, “High-speed in-line optical angular scatterometer for high-throughput roll-to-roll nanofabrication,” pp. 44–44, Feb. 2021, doi: https://doi.org/10.1117/12.2593730.

[10] J. Bai et al., “Normal incident optical reflectance spectroscopy for thin-film thickness measurement with genetic algorithm”, Measurement, pp. 118511–118511, Jul. 2025, doi: https://doi.org/10.1016/j.measurement.2025.118511.

[11] A. G. Marrugo, F. Gao, and S. Zhang, “State-of-the-art active optical techniques for three-dimensional surface metrology: a review [Invited],” JOSA A, vol. 37, no. 9, pp. B60–B77, Sep. 2020, doi: https://doi.org/10.1364/JOSAA.398644.

[12] D.-H. Cho, S. B. Park, S.-H. Kim, T. Kim, and K. Lee, “High-speed wafer film measurement with heterogeneous optical sensor system,” Metrology, Inspection, and Process Control for Semiconductor Manufacturing XXXV, p. 11, Feb. 2021, doi: https://doi.org/10.1117/12.2584200.

[13] J. Lauri, C. Liedert, and T. Fabritius, “Wavelength Scanning Interferometry for Topography of Microchannels at Roll-to-Roll Line with Optical Coherence Tomography,” 2022 IEEE International Instrumentation and Measurement Technology Conference (I2MTC), pp. 1–6, May 2021, doi: 10.1109/i2mtc50364.2021.9460091.

[14] J. Lauri, C. Liedert, R. Liedert, and T. Fabritius, “Online quality assurance of microchannels in Roll-to-Roll by optical coherence tomography,” 2022 IEEE International Instrumentation and Measurement Technology Conference (I2MTC), pp. 1–5, May 2020, doi: 10.1109/i2mtc43012.2020.9128465.

[15] T. Santoso, W. P. Syam, S. Darukumalli, and R. Leach, “Development of a compact focus variation microscopy sensor for on-machine surface topography measurement,” Measurement, vol. 187, p. 110311, Oct. 2021, doi: 10.1016/j.measurement.2021.110311.

[16] E. Grau-Luque et al., “Thickness evaluation of AlOx barrier layers for encapsulation of flexible PV modules in industrial environments by normal reflectance and machine learning,” Progress in Photovoltaics: Research and Applications, vol. 30, no. 3, pp. 229–239, Oct. 2021, doi: https://doi.org/10.1002/pip.3478.

[17] D.-H. Cho, S. B. Park, S.-H. Kim, T. Kim, and K. Lee, “High-speed wafer film measurement with heterogeneous optical sensor system,” Metrology, Inspection, and Process Control for Semiconductor Manufacturing XXXV, p. 11, Feb. 2021, doi: https://doi.org/10.1117/12.2584200.

[18] J. Park, Y. J. Cho, Won Chegal, J. Lee, Y.-S. Jang, and J. Jin, “A Review of Thin-film Thickness Measurements using Optical Methods,” International Journal of Precision Engineering and Manufacturing, Jun. 2024, doi: https://doi.org/10.1007/s12541-024-00955-3.

[19] Cheng, X., Tang, Y., Yang, K., and Han, C. (2022). Deep learning for thin film thickness measurement in spectroscopic reflectometry. IEEE Photonics Technology Letters, 34(18), 969–972.

[20] R. Xue, H. Hooshmand, M. Isa, S. Piano, and R. K. Leach, “Applying machine learning to optical metrology: a review,” Measurement Science and Technology, Sep. 2024, doi: 10.1088/1361-6501/ad7878.

[21] Z. Qu, W. Wang, X. Li, Q. Li and Y. Zheng, ”Measurement and Error Analysis of Cu Film Thickness With Ta Barrier Layer on Wafer for CMP Application,” in IEEE Transactions on Instrumentation and Measurement, vol. 70, pp. 1-10, 2021, Art no. 8000410, doi: 10.1109/TIM.2020.3017057.

[22] L. G. Connolly, T.-F. Yao, A. Chang, and M. Cullinan, “A tip-based metrology framework for real-time process feedback of roll-to-roll fabricated nanopatterned structures,” Precision Engineering, vol. 57, pp. 137–148, Apr. 2019, doi: https://doi.org/10.1016/j.precisioneng.2019.04.001.

[23] G. Gurbandurdyyev et al., “Robust, Conformal ZnO Coatings on Fabrics via Atmospheric-Pressure Spatial Atomic Layer Deposition with In-Situ Thickness Control,” ChemNanoMat, vol. 9, no. 2, Dec. 2022, doi: https://doi.org/10.1002/cnma.202200498.

[24] K. Mistry, A. Jones, M. Kao, T. W.-K. Yeow, M. Yavuz, and K. P. Musselman, “In-situ observation of nucleation and property evolution in films grown with an atmospheric pressure spatial atomic layer deposition system,” Nano Express, vol. 1, p. 010045, June 2020.

[25] N. E. Sánchez-Arriaga, D. Tiwari, W. Hutabarat, A. Leyland, and A. Tiwari, “A spectroscopic reflectance-based low-cost thickness measurement system for thin films: Development and testing,” Sensors, vol. 23, p. 5326, June 2023.

[26] A. C. Da Silva, J. Wang, and I. R. Minev, “Electro-assisted printing of soft hydrogels via controlled electrochemical reactions,” Nature Communications, vol. 13, no. 1, Mar. 2022, doi: https://doi.org/10.1038/s41467-022-29037-6.

[27] O. Heavens, Optical Properties of Thin Film Solids. New York: Dover Publications, 1991. ISBN 9780486669243

[28] M. Quinten, A Practical Guide to Optical Metrology for Thin Films. Wiley, Sep. 24, 2012. doi: 10.1002/9783527664344.

[29] L. Carlone, “Lecture 17-18: Least squares optimization,” accessed on 04-10-2024. https://vnav.mit.edu/material/17-18-NonLinearLeastSquares-notes.pdf.

[30] A. Bärligea and Juli, “Abschlussarbeit im Bachelorstudiengang Physik Assessment of a Variable Projection Algorithm for Trace Gas Retrieval in the Short-Wave Infrared.” Accessed: Apr. 16, 2025. [Online]. Available: https://elib.dlr.de/191480/1/Bachelorarbeit_Adelina_Baerligea.pdf

[31] S. F. Rahman, “Dynamic Dark Energy Equation of State (EoS) and Hubble Constant Analysis Using Type Ia Supernovae from Union 2.1 Dataset,” Astronomy Reports, vol. 64, no. 4. Pleiades Publishing Ltd, pp. 281–294, Apr. 2020. doi: 10.1134/s1063772920040046.

[32] C. Voglis and I. E. Lagaris, “A Rectangular Trust-Region Approach for Unconstrained and Box-Constrained Optimization Problems,” International Conference of Computational Methods in Sciences and Engineering 2004 (ICCMSE 2004). CRC Press, pp. 562–565, Apr. 29, 2019. doi: 10.1201/9780429081385-138.

[33] Desai, A. and Mital, A., ”Sustainable product design and development”, cg. 6, pp. 251, Boca Raton, FL: CRC Press, 1st ed., 2021.doi: https://doi.org/10.1201/9780429327803.

[34] N. Cross, “Engineering design methods: Strategies for product design,” in Generating Alternatives, ch. 10, NJ, USA: John Wiley and Sons Ltd, 5th ed., 2021.

[35] Supplyframe, “c12666ma Footprint, Symbol and 3D Model search results,” Component Search Engine, 2020. https://componentsearchengine.com/search?term=c12666ma

[36] E. Segerstrom, L. Vanfretti, C. Mishra, X. Xu, K. D. Jones, and R. M. Gardner, “Using Spectral Flatness to Detect and Label Power System Oscillations in the Presence of Intermittent Broadband Noise,” 2021 IEEE

Power & Energy Society General Meeting (PESGM), pp. 1–5, Jul. 2022, doi: https://doi.org/10.1109/pesgm48719.2022.9917166.

[37] L. Monroy, A. Pérez-Serrano, G. Tijero, and I. Esquivias, “Multi-gas dual-comb spectroscopy with tunable gain-switched laser diodes,” Scientific Reports, vol. 15, no. 1, Mar. 2025, doi: https://doi.org/10.1038/s41598-025-90108-x.

[38] Groupgets, “GitHub - groupgets/c12666ma,” GitHub, 2015. https://github.com/groupgets/c12666ma (accessed Aug. 22, 2025).

[39] Filmetrics, “Refractive index database,” accessed 15-05-2024. https://filmetrics.com/refractive-index-database.

[40] M. N. Polyanskiy, “Refractiveindex.info database of optical constants,” Scientific Data, vol. 11, Jan. 2024.

[41] Avantes, “Operation and installation manual avasoft user’s manual,” accessed on: 01-10-2024. https://www.avantes.com/support/downloads/software-1.

[42] Filmetrics, ”Operations Manual for the FILMETRICS F20 Thin-Film Analyzer”, accesed on: 19-08-2025. https://www.egr.msu.edu/psp/sites/default/files/content/F20%20User%20Manual.pdf

[43] N. E. Sánchez-Arriaga, D. Tiwari, W. Hutabarat, A. Leylandand A. Tiwari, “Data set. A Miniaturised Spectroscopic Reflectance System for Thin-Film Multilayer Thickness Measurements”. The University of Sheffield, 07-Mar-2025, doi: 10.15131/shef.data.28557008.

[44] National Physical Laboratory, “Manufacturer Measurement Network - An Introduction to Sensor Validation,” YouTube, Jun. 21, 2023. https://www.youtube.com/watch?v=owVJMacNq4w (accessed Apr. 17, 2025).

[45] M-G. Kim, “Improved Measurement of Thin Film Thickness in Spectroscopic Reflectometer Using Convolutional Neural Networks,” International Journal of Precision Engineering and Manufacturing, vol. 21, no. 2, pp. 219–225, Oct. 2019, doi: https://doi.org/10.1007/s12541-019-00260-4.

[46] National Physical Laboratory, “Beginner’s guide to measurement GPG118 - NPL,” Npl.co.uk, accessed on 30-08-2025. https://www.npl.co.uk/resources/gpgs/beginners-guide-to-measurement

[47] Hamamatsu, “Mini-spectrometers Technical Information”, Hamamatsu city, 2024, accessed on 30-08-2025: https://www.hamamatsu.com/content/dam/hamamatsu-photonics/sites/documents/99_SALES_LIBRARY/ssd/mini-spectrometer_kacc9003e.pdf

[48] I. Ohlídal, Jiří Vohánka, J. Dvořák, V. Buršíková, and Petr Klapetek, “Determination of Optical and Structural Parameters of Thin Films with Differently Rough Boundaries,” Coatings, vol. 14, no. 11, pp. 1439–1439, Nov. 2024, doi: https://doi.org/10.3390/coatings14111439.

[49] A. C. Da Silva, T. E. Paterson, and I. R. Minev, ‘Electro-assisted assembly of conductive polymer and soft hydrogel into core-shell hybrids’, Soft Science, vol. 3, no. 1. OAE Publishing Inc., p. 3, 2023. doi: 10.20517/ss.2022.25.

[50] A. C. Da Silva et al., ‘Electrochemically Driven Assembly of Chitosan Hydrogels on PEDOT Surfaces’, Macromolecular Materials and Engineering, vol. 309, no. 2. Wiley, Sep. 20, 2023. doi: 10.1002/mame.202300263.

BIOGRAPHY SECTION

Néstor Eduardo Sánchez-Arriaga received a B.Eng. degree in electronics from the Universidad Autónoma de Tamaulipas, México (2007); and a master’s degree in IT management from the Universidad TecMilenio, México (2012), before obtaining the PhD degree from The University of Sheffield (UK) in 2025. Before joining academia, he worked in engineering and leadership roles in manufacturing and product development for global telecommunications companies.

Aruã Clayton, Da Silva holds a B.Sc. in Chemistry from the State University of Londrina (2013). He served as a Visiting Researcher at the University of Wollongong, Australia (2017–2018) and earned his Ph.D. in Science from the University of São Paulo (2020), with honours in 2021. From 2020 to 2024, he worked as an Associate Researcher on Implantable Bioelectronic Systems at the University of Sheffield. He is a Research Fellow at the University of Limerick, Ireland, focusing on developing hydrogel-based sealant systems.

Divya Tiwari received the B.Eng. degree in electronics and communication in 2002, and the Ph.D. degree from Cranfield University in 2010. Before joining academia, she worked in the electronics industry on aerospace and automotive applications in the U.K. She is a Research Fellow working with the Digitisation Laboratory for Manufacturing at The University of Sheffield. Her work focuses on sensors and simulation for high-value manufacturing processes. She was awarded the Daphne Jackson and Royal Academy of Engineering Fellowship in 2013.

Windo Hutabarat received an aeronautical B.Eng. degree in 2001. He worked in the aviation industry before joining academia. He is a Research Associate at the University of Sheffield. He is part of the Airbus/RAEng Research Team in Digitisation of Manufacturing and is an Application Research Lead with the EPSRC Made Smarter Research Centre for Connected Factories. He is a part-time Doctoral Student. He has extensive research experience collaborating with U.K. industries.

Adrian Leyland is an Honours Graduate of Leeds University (BSc, Materials Science & Engineering, 1985). He joined the Department of Materials at Sheffield in 2003, having spent 17 years at Hull University, where he obtained his PhD in Plasma Surface Engineering in 1992. Dr. Leyland has over 35 years of experience in applied Surface Engineering and Tribology research - particularly in the development of PVD coatings, plasma thermochemical surface treatments, duplex & hybrid coating/treatments, and the implementation & standardisation of coating test methods.

Ashutosh Tiwari is a Deputy Vice-President for Innovation at the University of Sheffield and holds the prestigious Royal Academy of Engineering (RAEng) and Airbus Research Chair. He is internationally renowned for research in digital manufacturing and works in partnership with industry to develop new techniques and solutions for digitalisation, instrumentation, in-process monitoring and real-time simulation of skill-intensive manufacturing processes. He has a strong track record of leading research and innovation projects across technology readiness levels, and serves on the Engineering and Physical Sciences Research Council (EPSRC) Strategic Advisory Team for Manufacturing and the Circular Economy. He is the Deputy Director of the EPSRC Future Electrical Machines Manufacturing Hub, Sheffield Lead of the Made Smarter Research Centre for Connected Factories, and was awarded an EPSRC High-Value Manufacturing Catapult Fellowship. He is passionate about training people for manufacturing research and has graduated 38 Ph.D. students.